Chemical Engineering Journal

FeS2/MoS2@RGO hybrid materials derived from polyoxomolybdate-based metal-organic frameworks as high-performance electrocatalyst for ammonia synthesis under ambient conditions

--Manuscript Draft--

Manuscript Number:	
Article Type:	Research Paper
Section/Category:	Novel Materials for Energy and Advanced Applications
Keywords:	polyoxometalates, metal-organic frameworks, bimetallic sulfide, electrocatalysts, nitrogen reduction reaction
Corresponding Author:	huiyuan ma, Ph.D Harbin University of Science and Technology Harbin, CHINA
First Author:	huiyuan ma, Ph.D
Order of Authors:	huiyuan ma, Ph.D
	Zemin Feng
	Xinming Wang
	Carlos J Gómez-García
	Jianjiao Xin
	Haijun Pang
	Keqing Gao
Abstract:	The electrocatalytic nitrogen reduction reaction (NRR) provides a promising way for storage and sustainable utilization of ammonia. In order to reduce the cost of ammonia synthesis and promote large-scale production, it is very important to develop stable and highly active electrocatalysts. In this work, we demonstrate an iron-based metal-organic framework (MIL-100) and molybdenum-based polyoxometalate (PMo 12) host-guest-assisted strategy for synthesizing nanostructured bimetallic sulfides through a one-pot hydrothermal synthesis process. FeS 2 /MoS 2 particles are evenly distributed on reduced graphene oxide (RGO) with high conductivity, forming a well-defined nanoflower structure. Benefiting from the synergistic effect of FeS 2 , MoS 2 (with inherent rich catalytically active sites and uniform nanoflower structure) and RGO, the as-synthesized FeS 2 /MoS 2 @RGO achieves electrocatalytic activity and stability towards NRR in both basic and acidic solutions. The electrochemical results show a high Faradaic efficiency (FE) of 38.6 % and NH 3 yield rate of 41.1 μ g h -1 mg cat -1 at -0.2 V with respect to a reversible hydrogen electrode (RHE) in acidic potassium sulfate, and FE of 9.62 % and NH 3 yield rate of 10.35 μ g h -1 mg cat -1 at -0.4 V vs . RHE in alkaline potassium hydroxide solution at room temperature. We develop a general and promising method for the design of efficient and low cost pH-universal NRR electrocatalysts.
Suggested Reviewers:	Mohammad Rafiee Department of Chemistry, University of Missouri-Kansas City Rockhill Rd. Kansas City, MO 64110 mrafiee@umkc.edu
	Yangguang Li Key Laboratory of Polyoxometalate Science of the Ministry of Education, Faculty of Chemistry, Northeast Normal University, Changchun, China liyg658@nenu.edu.cn
	Zhiming Zhang Institute for New Energy Materials and Low Carbon Technologies, School of Materials Science & Engineering, School of Chemistry and Chemical Engineering, Tianjin University of Technology, Tianjin 300384, China

	zmzhang@email.tjut.edu.cn
Opposed Reviewers:	

Huiyuan Ma, Ph.D.
Professor

Harbin University of Science and Technology
4, Linyuan Road, Xiangfang District
Harbin 150040 China
Telephone: 86-451-86392716
Email: mahy017@163.com

03/11/2021

Chemical Engineering Journal Editorial Board

Dear Editor,

We submit our manuscript titled "FeS_2/MoS_2@RGO hybrid materials derived from polyoxomolybdate-based metal-organic frameworks as high-performance electrocatalyst for ammonia synthesis under ambient conditions" to ***Chemical Engineering Journal***.

In this manuscript, the main features are the following:

1.The polyoxometalate-based metal-organic framework with host-guest-structure is employed as self-template, the sulphuration process is confined within the POMs-based MOF matrix, preventing the combination and growth of the in situ-generated sulfide nanocrystallites, and promoting the formation of multi-interfacial iron and molybdenum disulfides inserted the reduced graphene oxide composite (shorted as **FeS_2/MoS_2@RGO**).

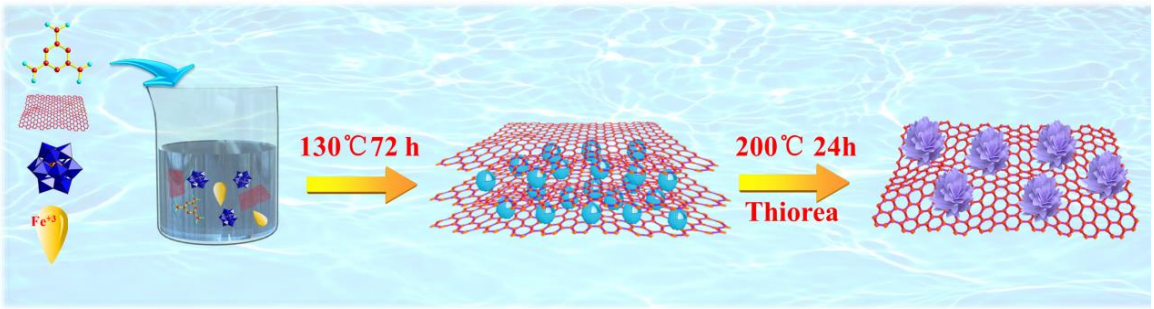

Scheme 1. The preparation of **FeS_2/MoS_2@RGO** composites.

2. As shown from SEM and TEM images of PMo_{12}@MIL-100(Fe)@RGO and **FeS_2/MoS_2@RGO** in **Figure 1a** and **1b**, the originally PMo_{12}@MIL-100(Fe) spherical precursor have all been converted to flower cluster-like FeS_2-MoS_2 uniformly dispersed on RGO. The TEM image of **FeS_2/MoS_2@RGO** (**Figure 1c and 1d**) demonstrates the flower cluster-like FeS_2-MoS_2 consist of the interconnected and staggered nanosheets, which would be beneficial for electron transfer and N_2 absorption. Elemental mapping

Huiyuan Ma, Ph.D.
Professor

Harbin University of Science and Technology
4, Linyuan Road, Xiangfang District
Harbin 150040 China
Telephone: 86-451-86392716
Email: mahy017@163.com

images of FeS_2-MoS_2@IF_{200} (**Figure 1e**) reveal that C, S, Fe, and Mo elements are uniformly distributed on the whole particles surface.

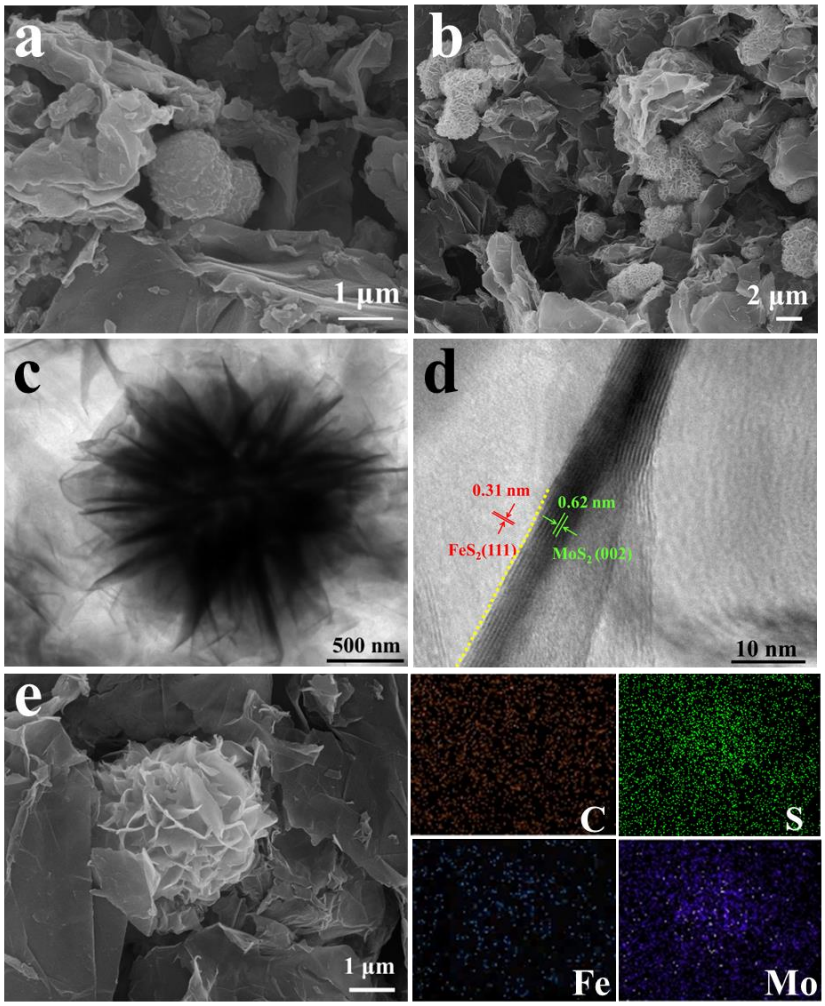

Figure 1. (a) SEM image of PMo_{12}@MIL-100(Fe)@RGO (15 % wt). (b) SEM image of **FeS_2/MoS_2@RGO** (15 % wt). (c) TEM image of **FeS_2/MoS_2@RGO** (15 % wt). (d) HRTEM images of **FeS_2/MoS_2@RGO** (15 % wt). (e) Elemental mapping of C, S, Fe and Mo on **FeS_2/MoS_2@RGO** (15 % wt).

Huiyuan Ma, Ph.D.
Professor

Harbin University of Science and Technology
4, Linyuan Road, Xiangfang District
Harbin 150040 China
Telephone: 86-451-86392716
Email: mahy017@163.com

3. The FeS_2/MoS_2@RGO (15% wt) exhibits an excellent NRR performance and stability in acidic and alkaline media. Especially, the largest NH_3 yield of 41.1 μg h^{-1} mg_{cat}^{-1} at –0.2 V (vs. RHE) under ambient conditions (**Figure 4**) are excellent to many transition-metal electrocatalysts in aqueous electrolytes (**Table S1**).

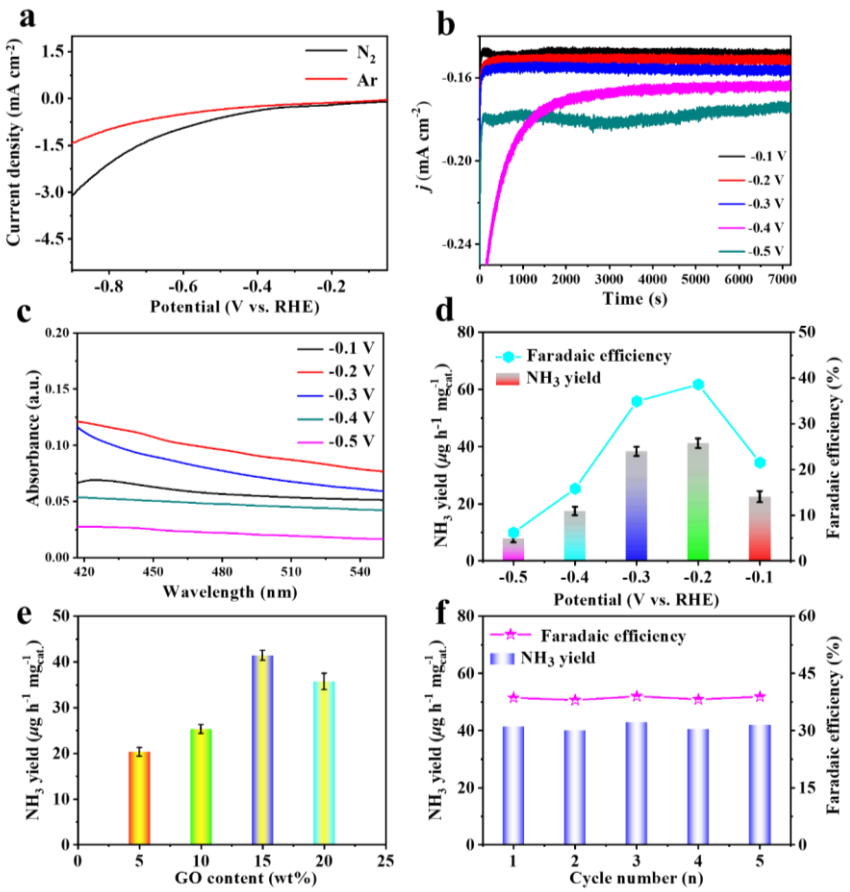

Figure 4. (a) LSV curves of **FeS_2/MoS_2@RGO** (15 % wt) in Ar- or N_2-saturated acidic potassium sulfate (pH 3.5, 1.0 M of K^+). (b) Amperometric *i-t* curves of **FeS_2/MoS_2@RGO** (15 % wt) for NRR (c) UV-vis curves of Nessler's reagent solutions after keeping in darkness for 30 min at room temperature. (d) NH_3 yield rate and FE of **FeS_2/MoS_2@RGO** (15 % wt) for NRR at different voltages. (e) The NH_3 yield rate of **FeS_2/MoS_2@RGO** (5, 10, 15 and 20 % wt) at -0.2 V *vs*. RHE. (f) The NH_3 yield rate and FE of **FeS_2/MoS_2@RGO** (15 % wt) at -0.2 V vs. RHE during five interval's cycles.

Huiyuan Ma, Ph.D.
Professor

Harbin University of Science and Technology
4, Linyuan Road, Xiangfang District
Harbin 150040 China
Telephone: 86-451-86392716
Email: mahy017@163.com

Table S1. Summary of part of representative NRR electrocatalysts reported in recent years and their catalytic performance

Catalysts	Electrolyte	FE (%)	Yield (NH_3) ($\mu g\ h^{-1}\ mg_{cat}^{-1}$)	Potential (V vs. RHE)	Ref.
FeS_2/MoS_2@RGO	pH 3.5, 1.0 M K^+	38.6	41.1	-0.2	
	0.1 M KOH	9.62	10.35	-0.4	**This**
FeS_2@RGO	pH 3.5, 1.0 M K^+	35.6	38.2	-0.3	**work**
MoS_2@RGO	pH 3.5, 1.0 M K^+	25.5	27.1	-0.3	
FeS_2	0.1 M Na_2SO_4	11.2	37.2	-0.5	5
Fe−N/C−CNT	0.1 M KOH	9.28	34.83	-0.2	6
Defect-rich MoS_2	0.1 M Na_2SO_4	8.34	29.28	-0.4	7
BNS	0.1 M Na_2SO_4	4.04	13.22	-0.8	8
MoS_2/BCCF	0.1 M Li_2SO_4	9.81	43.4	-0.2	9
MoS_2/C_3N_4	0.1 M $LiClO_4$	17.8	18.5	-0.3	10
MoFe-PC	0.1 M HCl	16.83	34.23	-0.5	11
SA-Mo/NPC	0.1 M KOH	14.6±1.6	34.0±3.6	-0.3	12
Mo_2C/C	0.5 M Li_2SO_4	7.8	11.3	-0.3	13
$FeMo_3S_4$	0.5 M $LiClO_4$	19.2	65.3	-0.3	14
Mo_3Fe_3C	0.1 M Li_2SO_4	27.0	1.232	-0.05	15
$CoMoO_4$ Nanorods	0.1 M Na_2SO_4	22.76	4.70×10^{-3}	-0.1	16
P-NV-C_3N_4	0.1 M Na_2SO_4	22.15	28.67	-0.3	17
Cu_2-xS/MoS_2-2.5%	0.1 M Na_2SO_4	6.06	22.1	-0.5	18
Au–Fe_3O_4 NPs	0.1 M KOH	10.54	21.42	-0.2	19
Bi_2MoO_6	0.1 M HCl	8.17	20.46	-0.6	20
NiFe-nanomesh array	0.1 M Na_2SO_4	12.5	16.89	-0.35	21

This work provides an ingenious way towards excellent FeMo-based bimetallic sulfide catalysts for nitrogen reduction.

Huiyuan Ma, Ph.D.
Professor

Harbin University of Science and Technology
4, Linyuan Road, Xiangfang District
Harbin 150040 China
Telephone: 86-451-86392716
Email: mahy017@163.com

The article is original, and we think that this manuscript is appropriate for publication in ***Chemical Engineering Journal***. We guarantee that this paper has not been published elsewhere, and we look forward to hearing from you for your decision at your earliest convenience.

Sincerely,

Prof. Huiyuan Ma

List of Suggested Reviewers

Yangguang Li
Key Laboratory of Polyoxometalate Science of the Ministry of Education, Faculty of Chemistry, Northeast Normal University, Changchun, China
E-mail: liyg658@nenu.edu.cn

Mohammad Rafiee
Department of Chemistry, University of Missouri-Kansas City
Rockhill Rd. Kansas City, MO 64110
E-mail: mrafiee@umkc.edu

Zhiming Zhang
Institute for New Energy Materials and Low Carbon Technologies, School of Materials Science & Engineering, School of Chemistry and Chemical Engineering, Tianjin University of Technology, Tianjin 300384, China
E-mail: zmzhang@email.tjut.edu.cn

Ping Xu
MIIT Key Laboratory of Critical Materials Technology for New Energy Conversion and Storage, School of Chemistry and Chemical Engineering, Harbin Institute of Technology, Harbin 150001, China. Email: pxu@hit.edu.cn

Yongge Wei
Department of Chemistry, Tsinghua University, Beijing, China
E-mail: yonggewei@mail.tsinghua.edu.cn

Graphical Abstract

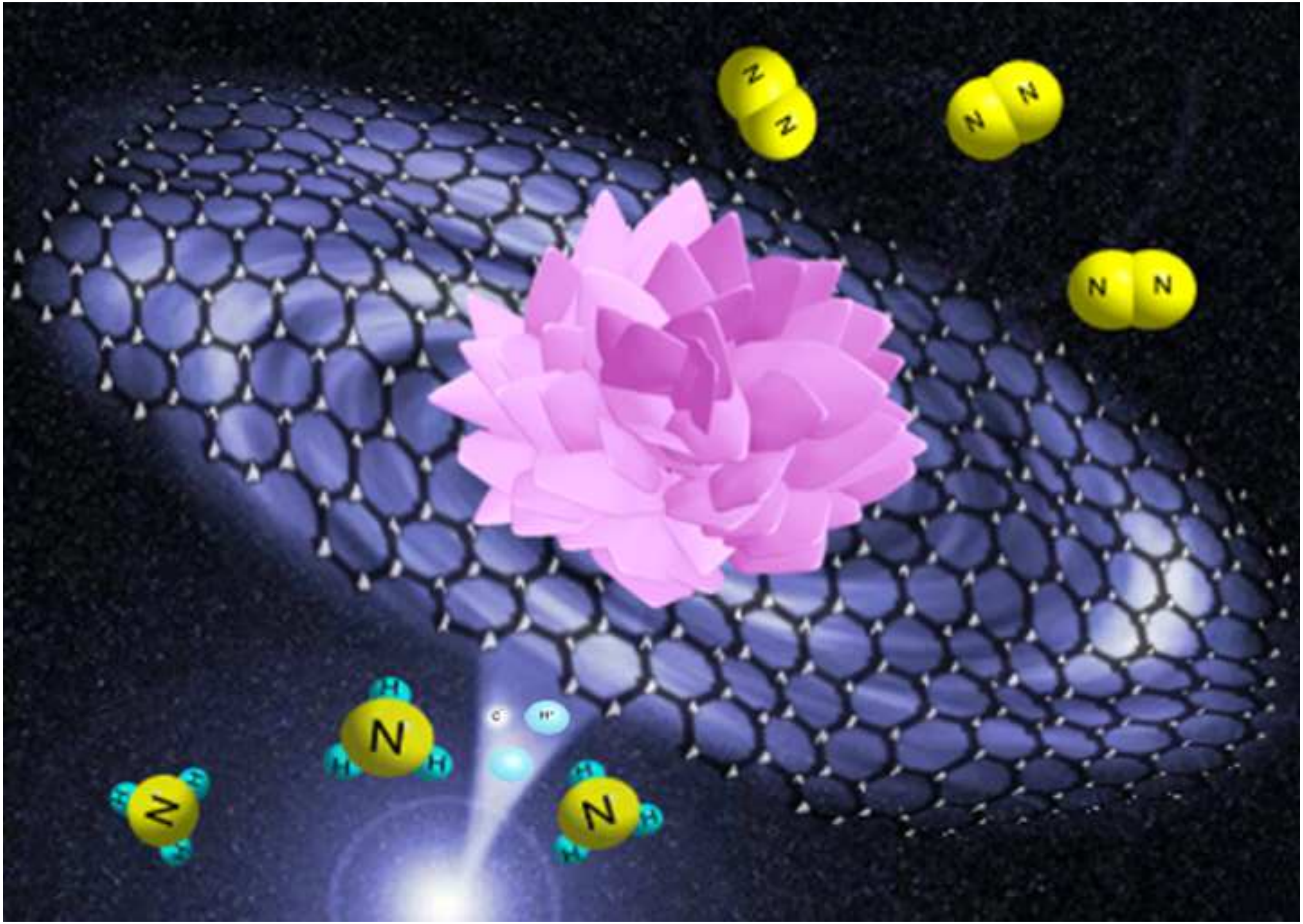

Highlights

- The polyoxometalate-based metal-organic framework with host-guest-structure is employed as self-template.
- FeS_2/MoS_2 nanoflower particles are uniformly dispersed on reduced graphene oxide matrix.
- The interconnected and staggered nanosheets in FeS_2/MoS_2 would be beneficial N_2 fixation and ammonia synthesis.
- FeS_2/MoS_2@RGO exhibits an excellent NRR performance and stability in acidic and alkaline media

FeS_2/MoS_2@RGO hybrid materials derived from polyoxomolybdate-based metal-organic frameworks as high-performance electrocatalyst for ammonia synthesis under ambient conditions

Zemin Feng[a], Xinming Wang[a,*], Carlos J. Gómez-García[b], Jianjiao Xin[a], Huiyuan Ma[a,*], Haijun Pang[a], Keqing Gao[c]

[a] College of Materials Science and Chemical Engineering, Harbin University of Science and Technology, Harbin, 150040, P. R. China.

[b]Instituto de Ciencia Molecular, Departamento de Química Inorgánica Universidad de Valencia C/Catedrático José Beltrán, 2, 46980 Paterna, Spain

[c] Beijing Caron Fiber Engineering Technology Research Center Beijing Bluestar Technical Center, Beijing 101318, P. R. China.

E-mail address: wangxinming20@126.com

E-mail address: mahy017@163.com

Abstract: The electrocatalytic nitrogen reduction reaction (NRR) provides a promising way for storage and sustainable utilization of ammonia. In order to reduce the cost of ammonia synthesis and promote large-scale production, it is very important to develop stable and highly active electrocatalysts. In this work, we demonstrate an iron-based metal-organic framework (MIL-100) and molybdenum-based polyoxometalate (PMo_{12}) host-guest-assisted strategy for synthesizing nanostructured bimetallic sulfides through a one-pot hydrothermal synthesis process. FeS_2/MoS_2 particles are evenly distributed on reduced graphene oxide (RGO) with high conductivity, forming a well-defined nanoflower structure. Benefiting from the synergistic effect of FeS_2, MoS_2 (with inherent rich catalytically active sites and uniform nanoflower structure) and RGO, the as-synthesized **FeS_2/MoS_2@RGO** achieves electrocatalytic activity and stability towards NRR in both basic and acidic solutions. The electrochemical results show a high Faradaic efficiency (FE) of 38.6 % and NH_3 yield rate of 41.1 μg h^{-1} mg_{cat}^{-1} at -0.2 V with respect to a reversible hydrogen electrode (RHE) in acidic potassium sulfate, and FE of 9.62 % and NH_3 yield rate of 10.35 μg h^{-1} mg_{cat}^{-1} at -0.4 V *vs.* RHE in alkaline potassium hydroxide solution at room temperature. We develop a general and promising method for the design of efficient and low cost pH-universal NRR electrocatalysts.

Keywords: polyoxometalates, metal-organic frameworks, bimetallic sulfide, electrocatalysts, nitrogen reduction reaction

Introduction

NH_3 is an important chemical materials for the production of dyes, explosives, and fertilizers, and is an promising non-carbon energy carrier.[1–4] So far, the main way of synthetic NH_3 is the energy consuming Haber−Bosch (HB) method.[5] People pay increasing attention to finding more effective and mild nitrogen fixation pathways such as nitrogenase catalysis,[6,7] plasma-induced method,[8] photocatalysis[9] and electrochemical catalysis.[10,11] Electrocatalytic N_2 reduction reaction is a promising way for electrochemical synthesis of NH_3 in these methods. The electrocatalysts based on noble metals, such as Au,[12] Pt,[13] Ru,[14] and Rh,[15] show favorable activities towards NRR. However, these noble metal-based catalysts hinder further development due to their low reserves. Considerable attention has been focused on earth-rich materials as high-effective electrocatalysts for reducing N_2 to NH_3 under ambient conditions,[16] in order to develop low-cost and high-performance NRR electrocatalysts, such as VN,[17] $Bi_4V_2O_{11}/CeO_2$,[18] Mo_2C/C,[19]…

The transition metal disulfides are one of the promising studied materials. The 2D phase of MoS_2 possesses a tri-layer S-Mo-S configuration with hexagonal symmetry, where the positively charged Mo atoms at the edge of MoS_2 are favorable for N_2 adsorption and capable of activating N_2 bonds for hydrogenation.[20] Nevertheless, the NRR performance with single MoS_2 is still very low due to the limited conductivity within the layers, poor activation of intermediates, low charge carrier density, and competitive H_2 evolution activity.[21] To fix these limitations, some other materials compounded with MoS_2 can improve NRR catalytic activity. For example, Chu *et al*.[22] reported a NRR catalyst composed of MoS_2 and C_3N_4 that shown a surprisingly improved NRR performance with an NH_3 yield of 18.5 μg h^{-1} mg^{-1} and a high Faradaic efficiency (FE) of 17.8 % at -0.3 V versus reversible hydrogen electrode (RHE). This performance is much better than those of the single C_3N_4 or MoS_2 components. Suryanto *et al.*[23] reported a highly selective Ru/MoS_2 NRR catalyst with a NH_3 yield rate of 1.14×10^{-10} mol cm^{-2} s^{-1} and FE of 17.6 %. Han *et al*.[24] demonstrated a MoS_2 nanodots-reduced graphene oxide hybrid (MoS_2 NDs/RGO) with a high FE of 27.93 % and corresponding NH_3 yield rate of 16.41 μg h^{-1} mg_{cat}^{-1}. Even if some improved MoS_2-based electrocatalysts of N_2 reduction as mentioned above have been obtained, the relative FE is still unsatisfactory and, therefore, the development of MoS_2-based composite electrocatalysts with high activity for the NRR, still remains a challenge.

The nitrogenase of biological nitrogen fixation in nature contains Fe-Mo related

proteins.[25] Meanwhile, the catalytic site of many enzymes (such as hydrogenase) is the part formed by Fe.[26] Hence the combination of Fe-based materials and MoS_2 could simulate natural systems effectively. Compared with the iron atom in natural nitrogenase, the earth-abundant and nontoxic FeS_2 has a similar coordination field structure [27] suggesting a great application potential as an active component to build less expensive and high-activity NRR catalysts. After modification and regulation, the synthesized FeS_2 with smaller size have better designability and better electrochemical properties. Therefore, combining MoS_2 and FeS_2 to form FeS_2-MoS_2-based bimetallic sulfide composites with a heterointerface should be a possible effective strategy to develop excellent NRR catalyst, where possible synergistic effects between Fe and Mo may boost the NRR performance. The MOFs structures offer particular benefits for the manufacture of metal-based nano materials and the MOFs-derived strategies are easy to obtain with controllable morphology. Therefore, many MOFs-derived metal-based materials have been reported (for instance, Co, Ni, and Zn).[28] In contrast to most of the previous reports, in this work we present a flexible synthetic strategy consisting in the confined sulphuration reaction of a MOF with guest polyoxometalates (POMs) located in its pores.

POMs are a well-defined class of early transition metal (TM)-oxido clusters (TM = Mo, V, W, etc.) with many possible compositions and structures that display good redox properties.[29-32] The early transition metal sulfides can be easily synthesized by introducing POMs into MOF as co-precursors.[33-35] Furthermore, the POMs are uniformly distributed and surrounded by the MOF frame in a confined nanoscale space, thereby guaranteeing the *in situ* sulphuration reaction and generating uniform nanocrystallites. Moreover, the sulphuration process is confined within the metal-organic matrix, preventing the combination and growth of the in situ-generated sulfide nanocrystallites, and promoting the formation of multi-interfacial composites. This strategy based on POMOFs-derived materials has been recently extended to MoO_2@PC-RGO,[36] Fe_3C/Mo_2C@NPGC,[37] MoP@PPC,[38] etc. Only very recently, we have started to use Fe-based MOFs containing POMs as precursor to prepare FeMo-based electrocatalysts ($Fe_{1.89}Mo_{4.11}O_7/FeS_2$@C) and achieved an atomic-scale mixture of Mo and Fe.[39] We can, therefore, conclude the POMOFs are expected to be ideal precursors for the design and synthesis of metal-based electrocatalysts.

Motivated by these considerations, here we report a novel composite of iron and molybdenum disulfides inserted in the reduced graphene oxide matrix (shorted as **FeS_2/MoS_2@RGO**). This composite was prepared with a polyoxomolybdate-based iron-based MOF@RGO (PMo_{12}@MIL-100@RGO) through a feasible hydrothermal strategy.

The resulting **FeS_2/MoS_2@RGO** electrocatalyst has two main characteristics: (1) An atomic homogeneous distribution of Fe and Mo atoms with a multi-interface structure, formed thanks to the homogeneous mixture present in the precursor PMo_{12}@MIL-100(Fe) (the mesoporous cage of MIL-100(Fe) contains PMo_{12} POMs); (2) An increased electronic conductivity and surface area, thanks to the inclusion of the graphene substrates into these materials, resulting in a much easier electron transfer. Benefiting from the multi-component and multi-interface composite structure, the as-prepared **FeS_2/MoS_2@RGO** hybrid electrocatalyst exhibits a NH_3 yield rate of 41.1 μg h^{-1} mg_{cat}^{-1} with a FE of 38.6 % at -0.2 V *vs*. RHE in acidic potassium sulfate and a NH_3 yield rate of 10.35 μg h^{-1} mg_{cat}^{-1} with a FE of 9.62 % at -0.4 V *vs*. RHE in alkaline potassium hydroxide solution at room temperature. Furthermore, this **FeS_2/MoS_2@RGO** hybrid electrocatalyst also exhibits a high electrochemical stability. This facile strategy is also suitable for the synthesis of other early transition metals-based composite materials with W and V.

2. Results and discussion

2.1 Preparation of FeS_2/MoS_2@RGO catalytic materials

The **FeS_2/MoS_2@RGO** composite was synthesized via a two-step method as shown in Scheme 1. Firstly, the precursor PMo_{12}@MIL-100(Fe)@RGO (with GO loadings of 5, 10, 15 and 20 % wt) is synthesized *in situ* by a hydrothermal method. Then PMo_{12}@MIL-100(Fe)@RGO and thiourea are transferred to a Teflon-lined autoclave and heated in an oven at 200 °C for 24 h, leading to the formation of RGO that acts as a self-standing substrate for the growth of the FeS_2/MoS_2 nanoflowers (relevant information in the Supporting Information). The presence of Mo and Fe intimately mixed in the precursor PMo_{12}@MIL-100(Fe) facilitates the formation of the composite **FeS_2/MoS_2@RGO** with a multi-interface structure. The presence of the conductive graphene substrate into FeS_2/MoS_2-based material not only improves the conductivity but also increases surface area, and thus accelerates the electron transfer and facilitates the NRR. As a contrast, **MoS_2@RGO** and **FeS_2@RGO** were also prepared, as shown in the supporting information.

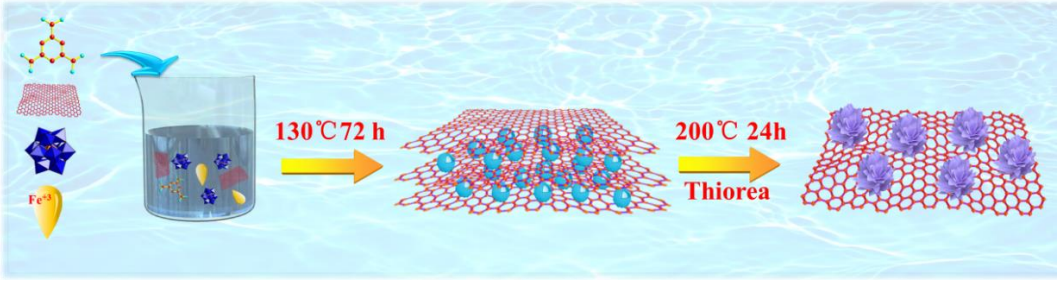

Scheme 1. The preparation of **FeS_2/MoS_2@RGO** composites.

Material characterization

The morphology and composition of as-prepared **FeS_2/MoS_2@RGO** are analyzed by field-emission scanning electron microscopy (SEM) and transmission electron microscopy (TEM). The SEMs images (Figure S1) of **FeS_2/MoS_2@RGO** composites derived from different precursors with 5, 10, 15 and 20 % wt GO, show that the composite with 15 % wt GO exhibits the most homogeneous distributions. Additionally, the SEMs images of PMo_{12}@MIL-100(Fe)@RGO (15 % wt) and **FeS_2/MoS_2@RGO** (15 % wt) show that the PMo_{12}@MIL-100(Fe) precursor forms spheres with a diameter around 1 µm scattered in RGO (Figure 1a). After sulfurization at 200 °C, these PMo_{12}@MIL-100(Fe) spheres give rise to FeS_2/MoS_2 nanoflower-like particles uniformly dispersed on RGO (Figure 1b). The TEM images of the final **FeS_2/MoS_2@RGO** (15 % wt) composite shows the microstructure feature of its nanoflowers (Figure 1c). Furthermore, high-resolution TEM (HRTEM) images reveal well-defined fringe spacings of 0.62 nm corresponding to the (002) lattice plane of MoS_2, and 0.31 nm belonging to the (111) plane of FeS_2 (Figure 1d). The elemental mapping images of the **FeS_2/MoS_2@RGO** (15 % wt) (Figure 1e) show the homogeneous distribution of C, S, Fe and Mo over the whole flower-like structure and further proves the composition of the **FeS_2/MoS_2@RGO** composite.

For comparative purposes, we have prepared **MoS_2@RGO** and **FeS_2@RGO** by sulphuration of PMo_{12}@GO (15 % wt) and MIL-100(Fe)@RGO (15 % wt) (Figures S3a), respectively (for synthesis details, see the supporting information). Their SEM, TEM, HRTEM and elemental mapping images are shown in Figures S2 and S3. The MoS_2/RGO composite shows well-defined nanoflower morphology (Figures S2a and S2b), whereas **FeS_2@RGO** exhibits a cauliflower-like morphology formed by the assembling of nanoflakes (Figures S3b and S3c). Their HRTEM shows the lattice fringes with distances of 0.62 nm in **MoS_2@RGO**, indexed as the (002) facet of MoS_2 (Figure S2c), and 0.27 nm in **FeS_2@RGO**, assigned to the (200) plane of the FeS_2 phase (Figure S3d). Their elemental mapping images (Figures S2d and S3e) prove the presence of C, S and Mo in the nanoflower of **MoS_2@RGO** and C, S and Fe in **FeS_2@RGO**.

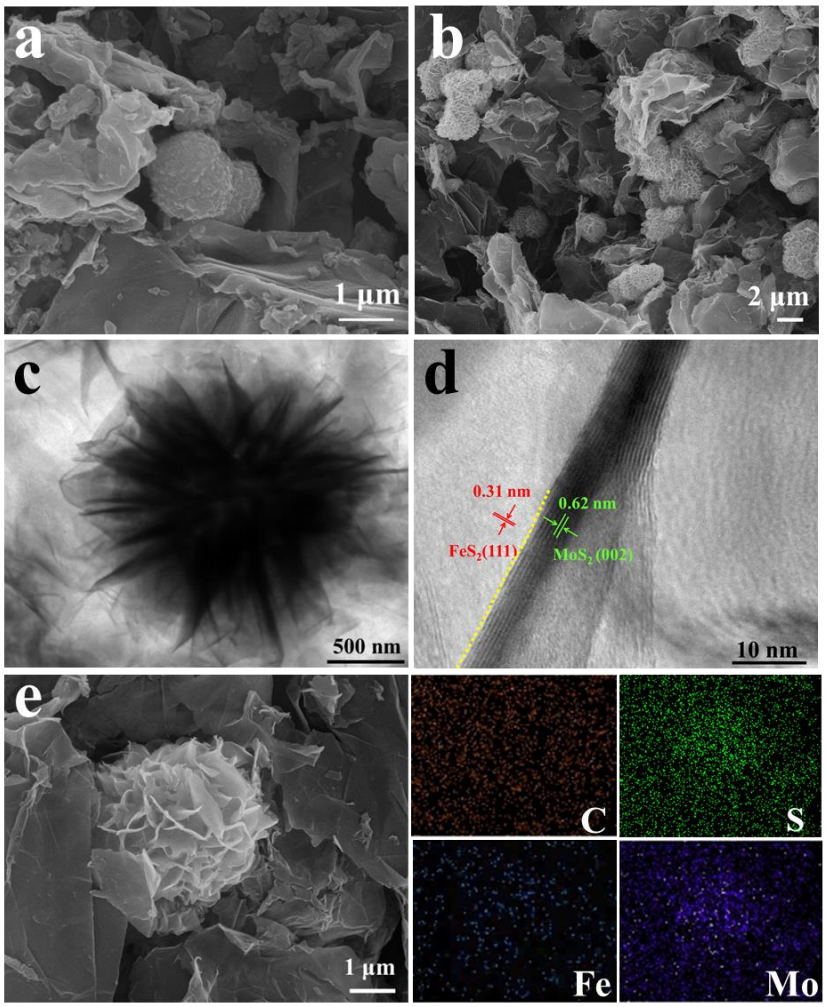

Figure 1. (a) SEM image of PMo_{12}@MIL-100(Fe)@RGO (15 % wt). (b) SEM image of **FeS_2/MoS_2@RGO** (15 % wt). (c) TEM image of **FeS_2/MoS_2@RGO** (15 % wt). (d) HRTEM images of **FeS_2/MoS_2@RGO** (15 % wt). (e) Elemental mapping of C, S, Fe and Mo on **FeS_2/MoS_2@RGO** (15 % wt).

The X-ray power diffraction (XRPD) patterns were also recorded to check for the crystal phase and composition of the different samples. As shown in Figure 2a, the XRPD pattern shows that the **FeS_2/MoS_2@RGO** composite contains a mixture of the individual FeS_2 and MoS_2 phases, with diffraction peaks at 28.51°, 33.08°, 37.10°, 40.78°, 47.41°, 50.49° and 56.28°, attributed to the (111), (200), (210), (211), (220), (221) and (311) lattice planes of the FeS_2 phase, respectively (JCPDS, no. 42-1340), and diffraction peaks at 14.38°, 29.03°, 32.67°, 33.51°, 35.87°, 39.54°, 58.33° and 60.14° corresponding to the (002), (004), (100), (101), (102), (103), (110) and (008) lattice planes of the crystalline MoS_2 phase, respectively (JCPDS, no. 37-1492). As can be seen in Figure 2b, all the **FeS_2/MoS_2@RGO** samples derived from the PMo_{12}@MIL-100(Fe)@RGO precursor show similar XRPD patterns, with

all the characteristic diffraction peaks matching the standard diffraction patterns, confirming that all the composites contain a mixture of FeS_2 and MoS_2 pure phases. Additionally, we have also measured the XRPD pattern of the two samples prepared for comparison purposes (**FeS_2@RGO** and **MoS_2@RGO**). These diffractograms show that they contain the pure FeS_2 and MoS_2 phases, respectively (Figure S4).

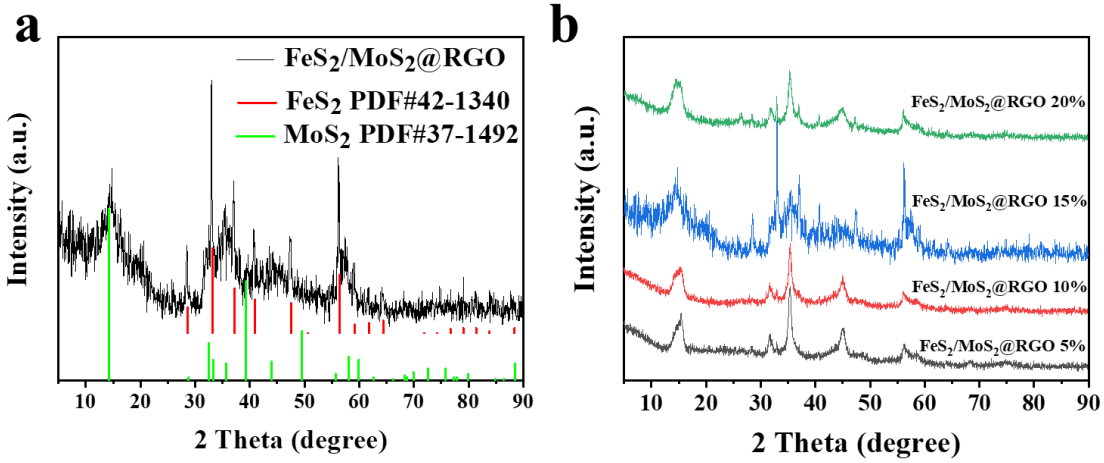

Figure 2. (a) XRPD patterns of **FeS_2/MoS_2@RGO**. (b) The comparative X-Ray powder diffractogram of **FeS_2/MoS_2@RGO** with different amounts of GO (5, 10, 15, 20 % wt) in the precursors.

Additional characterization was performed with X-ray photoelectron spectroscopy (XPS) measurements to evaluate the surface elemental composition and chemical oxidation states of **FeS_2/MoS_2@RGO**, **MoS_2@RGO**, and **FeS_2@RGO**. As can be seen in the XPS survey scan spectrum, the surface of the **FeS_2/MoS_2@RGO** (15 % wt) composite only contains C, S, O, N, Fe, and Mo (Figure S5). The high-resolution spectrum of C 1s has a strong peak of C=C/C-C species (284.6 eV) and two relatively weak peaks of C-N (285.7 eV) and C=O (288.5 eV) (Figure 3a). Compared to the two S 2p peaks in XPS spectra of **FeS_2@RGO** (162.5 eV for S $2p_{3/2}$ and 163.7 eV for S $2p_{1/2}$) (Figure S6) and **MoS_2@RGO** (162.0 eV for S $2p_{3/2}$ and 163.1 eV for S $2p_{1/2}$) (Figure S7), the S 2p peak of the **FeS_2/MoS_2@RGO** composite in Figure 3b splits into three peaks corresponding to Fe-S (162.1 eV), Mo-S $2p_{3/2}$ (163.9 eV) and Mo-S $2p_{1/2}$ (165.3 eV), whereas the peak at around 169 eV can be attributed to unsaturated S atoms. [40] It is noticeable the peak shapes changes for S 2p, that can be attributed to the occurrence of interfacial electronic interactions in **FeS_2/MoS_2@RGO**.[41] In the O 1s spectrum (Figure 3c) there are four peaks located at 530.7, 531.4, 532.2 and 533.3 eV, corresponding to the C=O, C-O-N/C-O, Mo-O and C-OH bonds, respectively. In the N 1s region, there exists the pyridinic N (398.2 eV), graphic N (401.7 eV) and Mo 3p (394.7 eV)

peaks (Figure 3d). [42,43] As shown in Figure 3e, the two peaks centered at 710.5 eV and 725 eV could be assigned to Fe $2p_{3/2}$ and Fe $2p_{1/2}$,[44] respectively, and the two peaks located at 707.3 eV and 719.9 eV correspond to (Fe-S) $2p_{3/2}$ and (Fe-S) $2p_{1/2}$, respectively. Figure 3f shows one pair of peaks at 232.8 eV and 236.2 eV are assigned to Mo^{6+} $3d_{5/2}$ and Mo^{6+} $3d_{3/2}$. Besides, the Mo 3d region shows a weak peak of S 2s (227 eV). The four peaks related to Mo 3d located at 228.9, 232.1, 229.9, and 233.5 eV, corresponding to MoS_2 polymorphs with +4 oxidation states. Obviously, the Mo 3d peak with +4 oxidation states for the **FeS_2/MoS_2@RGO** around 228 eV are split into two peaks (228.9 eV and 229.9 eV) compared with that of **MoS_2@RGO** (228.8 eV), suggesting that the formation of the composite materials changes the interfacial electronic structure and that the chemical surrounding of the Mo atoms is changed due to the formation of the FeS_2-MoS_2 composite. Interestingly, this change in the Mo surrounding improves the activation and/or adsorption process of nitrogen or its related species.[45]

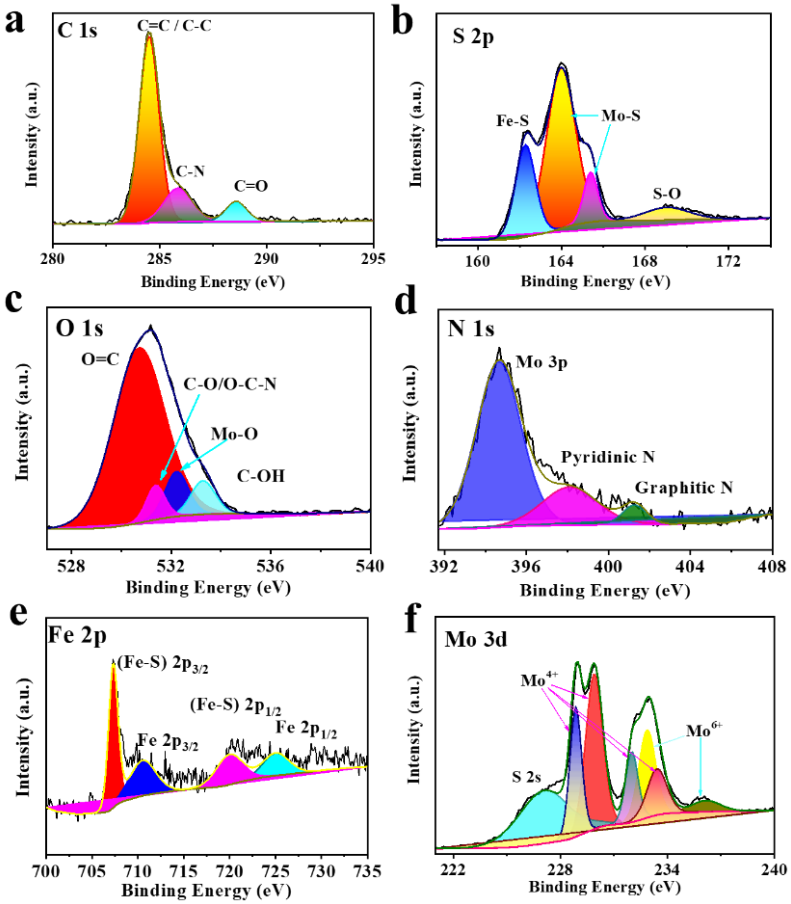

Figure 3. XPS spectra for **FeS_2/MoS_2@RGO** (15 % wt) in (a) C 1s, (b) S 2p, (c) O 1s, (d) N 1s, (e) Fe 2p, and (f) Mo 3d regions.

Electrochemical performances for NRR

We used an H-type electrolytic cell with a three electrodes device for NRR testing.[46] The carbon cloth loaded with catalyst is immersed in the electrolyte (pH 3.5, 1.0 M of K^+ or 0.1 M KOH) as working electrode. We purified the N_2 feeding gas by a saturator of 0.1 M HCl before introducing it into the electrolytic cell and each measured production of NH_3 was obtained from the corresponding fresh-prepared electrolyte. The purified N_2 was constantly bubbled into the cathode compartment with a flow rate of 30 cm^3 min^{-1}. We applied the Nessler's method[47] to analyze the generated NH_3 (see more details in the Supporting Information). The calibration curves for NH_3 are presented in Figures S8 and S9.

The linear sweep voltammetry (LSV) curves were measured in Ar- and N_2-saturated acidic potassium sulfate (pH 3.5, 1.0 M of K^+) to test the electrocatalytic activity of **FeS_2/MoS_2@RGO** for N_2 reduction (Figure 4a). When the potential is below -0.2 V *vs*. RHE, the current density of **FeS_2/MoS_2@RGO** (15 % wt) under N_2 clearly increases in comparison with the potential sweep under Ar, suggesting that the catalytic reduction of N_2 to NH_3 is taking place in this system. Because the H_2 formation could be restrain the NRR, to avoid the H_2 evolution, we have used potentials in the range -0.1 to -0.5 V for the electrochemical nitrogen fixation at **FeS_2/MoS_2@RGO** (15 % wt) in order to achieve the optimal performance in the NRR and no H_2 evolution. Figure 4b shows the chronoamperometry curves of **FeS_2/MoS_2@RGO** (15 % wt) after 2 h of the electrolytic reaction in the N_2-saturated solution at different working potentials. The Nessler's analysis shows that the highest yield rate and corresponding Faradaic efficiency (FE) of **FeS_2/MoS_2@RGO** (15 % wt) are achieved at -0.2 V *vs*. RHE, with values of 41.1 μg h^{-1} mg_{cat}^{-1} and 38.6 %. It is remarkable that the obtained NH_3 yield rate and FE are much better than many of the reported noble metal-based catalysts, such as Au_3Pd/NF (24.02 μg h^{-1} mg_{cat}^{-1} and 18.16 %),[48] PdRu TPs (37.23 μg h^{-1} mg_{cat}^{-1} and 1.85 %), [49] Ru@ZrO_2/NC (3 μg h^{-1} mg_{cat}^{-1} and 15 %), etc.[50] and many non-noble metal-based catalysts (For a more detailed and complete comparison see Table S1 in the supporting information).

In addition, the electrocatalytic activity of **FeS_2/MoS_2@RGO** (5, 10, and 20 % wt) at -0.2 V *vs*. RHE in acidic potassium sulfate were also explored (Figures 4e and S10). As can be seen in Figure 4e, **FeS_2/MoS_2@RGO** composites with 5 %, 10 %, and 20 % wt GO exhibit lower NH_3 yield rates (20.3, 25.3 and 35.7 μg h^{-1} mg_{cat}^{-1}, respectively) than the **FeS_2/MoS_2@RGO** composite with 15 % wt GO. This fact is probably due to the more uniform morphology and homogeneous distribution of the FeS_2/MoS_2 nanoflowers observed

in the **FeS_2/MoS_2@RGO** composite with 15 % wt GO (Figure S1). For low GO loadings, the nanoparticles/RGO ratio is very high, resulting in particle aggregation that reduces the catalytic surface and active sites. In contrast, when the GO loading is high, the nanoparticles/RGO ratio is too low, and the particle concentration decreases, also reducing the catalytic surface and active sites.

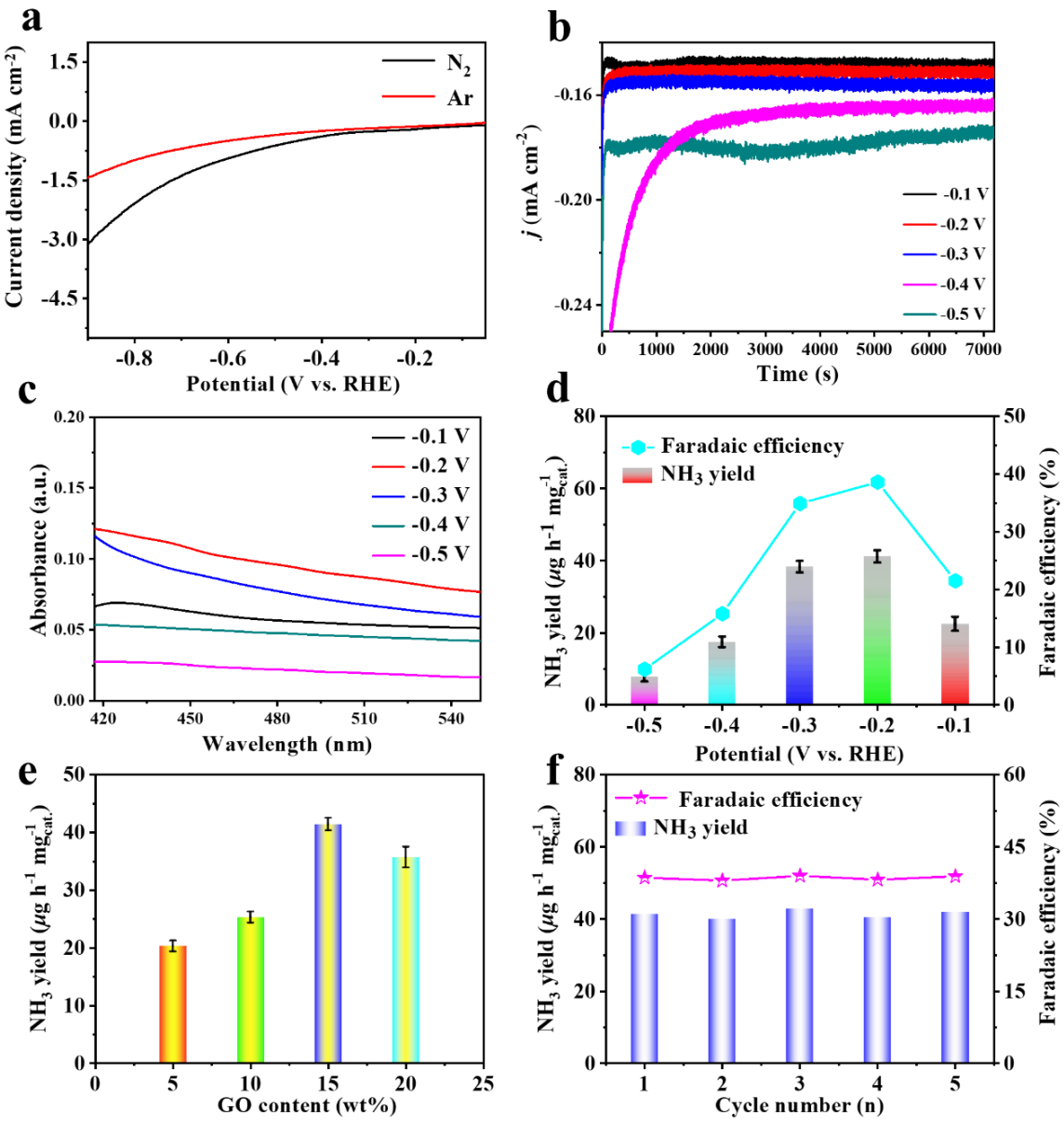

Figure 4. (a) LSV curves of **FeS_2/MoS_2@RGO** (15 % wt) in Ar- or N_2-saturated acidic potassium sulfate (pH 3.5, 1.0 M of K^+). (b) Amperometric *i-t* curves of **FeS_2/MoS_2@RGO** (15 % wt) for NRR (c) UV-vis curves of Nessler's reagent solutions after keeping in darkness for 30 min at room temperature. (d) NH_3 yield rate and FE of **FeS_2/MoS_2@RGO** (15 % wt) for NRR at different voltages. (e) The NH_3 yield rate of **FeS_2/MoS_2@RGO** (5, 10, 15 and 20 % wt) at -0.2 V *vs.* RHE. (f) The NH_3 yield rate and FE of **FeS_2/MoS_2@RGO** (15 % wt) at -0.2

V vs. RHE during five interval's cycles.

Since the **FeS_2/MoS_2@RGO** (15 % wt) exhibits the best NRR activity, we have selected this composite to perform a complete electrochemical characterization and catalytic study. For comparison, the NRR behaviors of the pure phases **FeS_2@RGO** and **MoS_2@RGO** were also evaluated. As can be seen in Figures S11, **FeS_2@RGO** presents a NH_3 yield rate of 38.2 μg h^{-1} mg_{cat}^{-1} (FE = 35.6 %) at -0.2 V *vs*. RHE, whereas **MoS_2@RGO** shows a NH_3 yield rate of 27.1 μg h^{-1} mg_{cat}^{-1} (FE = 25.5 %) at -0.3 V *vs*. RHE (Figure S12). Both composites exhibit lower NH_3 yield and FE than **FeS_2/MoS_2@RGO** (15 % wt) (Figure S13). These data clearly show that there is a synergy between FeS_2 and MoS_2 phases that increases the catalytic NRR performance of the **FeS_2/MoS_2@RGO** (15 % wt) composite.

Stability is one of the important indexes to evaluate the application performance of electrocatalysts. The test results (Figure 4f) of **FeS_2/MoS_2@RGO** (15 % wt) at -0.2 V *vs*. RHE with 2 h NRR for different recycling experiment show that both, the FE and NH_3 yield rate have no apparent change during five consecutive cycles, and its FE for producing NH_3 was always above 40.0 %. As depicted in Figure S14a, the durability test result of **FeS_2/MoS_2@RGO** (15 % wt) at -0.2 V *vs*. RHE shows that there is no obvious change in the current density after 10 h of NRR. Moreover, after the cycling tests, the **FeS_2/MoS_2@RGO** (15 % wt) composite retains its initial morphology (Figure S14b), indicating a good structural stability.

Additionally, we have also studied the NRR activity of the **FeS_2/MoS_2@RGO** (15 % wt) composite in alkaline media (0.1 M KOH). From Figure 5a, the NRR electrolysis tests were tested by using controlled potentials from -0.2 to -0.6 V *vs*. RHE for 2 h. A maximum FE of 9.62 % was achieved at -0.4 V *vs*. RHE and the corresponding NH_3 yield rate was 10.35 μg h^{-1} mg_{cat}^{-1}, as shown in Figure 5b and 5c. As observed in Figure 5d, the NH_3 yield rate and FE of **FeS_2/MoS_2@RGO** (15 % wt) present no apparent changes during five continuous cycles of N_2 reduction under the given conditions, indicating the high stability of **FeS_2/MoS_2@RGO** (15 % wt) for NRR in alkaline conditions. As expected, the NH_3 yield rate and FE of **FeS_2/MoS_2@RGO** (15 % wt) in the NRR in basic conditions are lower than those observed in acidic potassium sulfate. This lower yield and FE can be attributed to the much lower proton availability in basic medium, that is expected to limit the rate of the protonation steps during the NH_3 formation in the NRR.[51]

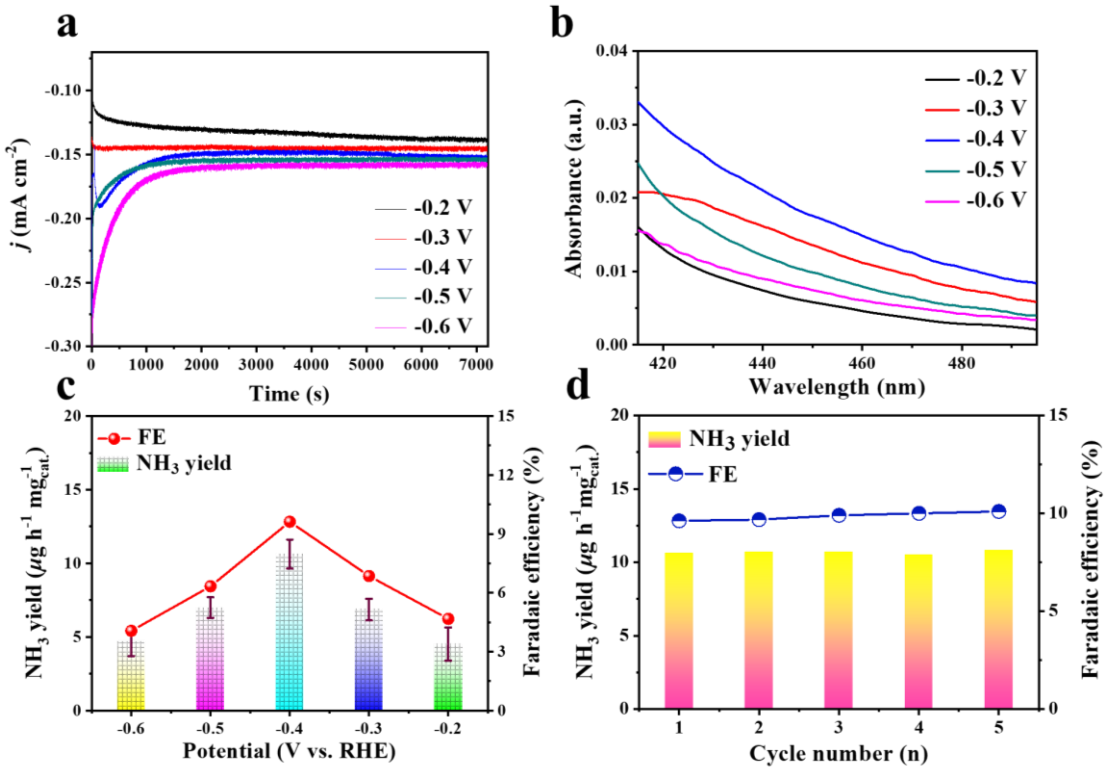

Figure 5. (a) Amperometric *i-t* curves of **FeS_2/MoS_2@RGO** (15 % wt) for NRR in 0.1 M KOH. (b) UV-vis curves of Nessler's reagent solutions after keeping in darkness for 30 min at room temperature in 0.1 M KOH. (c) NH_3 yield rate and FE of **FeS_2/MoS_2@RGO** (15 % wt) for NRR at different voltages in 0.1 M KOH. (d) Corresponding NH_3 yield rate and FE for five consecutive electrocatalysis cycles at -0.4 V *vs*. RHE in alkaline media.

In order to understand their different catalytic performances, we have measured the electrochemical active surface area (ECSA) of **FeS_2/MoS_2@RGO** (15 % wt), **FeS_2@RGO** and **MoS_2@RGO**. Figure S15 shows that the **FeS_2/MoS_2@RGO** (15 % wt) composite shows the double-layer capacitance value of 3.59 mF cm^{-2}, much higher than **FeS_2@RGO** (0.28 mF cm^{-2}) and **MoS_2@RGO** (0.22 mF cm^{-2}). These values suggest that **FeS_2/MoS_2@RGO** (15 % wt) possesses a much higher surface area with much more active sites to catalyze the N_2 reduction evolution reaction.[51] In addition, electrochemical impedance spectroscopy (EIS) measurement of electrocatalysts was carried out to test the electrocatalytic kinetics during the NRR process. The Nyquist plots in Figure S16 demonstrate that the **FeS_2/MoS_2@RGO** (15 % wt) composite has the lowest electron transport resistance among these catalyst materials, indicating that the charge redistribution at the FeS_2/MoS_2 interface could obviously boost charge transport and accelerate the NRR kinetics.

We have also measured the selectivity of **FeS_2/MoS_2@RGO** for NH_3 formation by

measuring the formation of N_2H_4 using the Watt and Chrisp method (Figure S17). This assay shows that no N_2H_4 is detected at any used potential (Figure S18), indicating an excellent selectivity of **FeS_2/MoS_2@RGO** for NH_3 formation. In order to detect possible sources of ammonia pollution, we did necessary controlling experiments on **FeS_2/MoS_2@RGO** (Figure S19 and Figure S20). The control experimental results demonstrate that N_2 gas, the electrolyte solution, the Nafion carbon cloth electrode nor the catalysts mixture are free from ammonia pollution over time. These experiments proved that the NH_3 in the electrolyte is exclusively produced via the NRR process using N_2 as the only N resource and **FeS_2/MoS_2@RGO** (15 % wt) as the catalyst.

Although the catalytic activity is better in acidic medium, the above measurements also show a NRR performance of **FeS_2/MoS_2@RGO** in a wide pH range. The following reasons may explain this remarkable electrocatalytic performance: (i) The partially occupied d-orbital of transition-metal species (Fe, Mo) in **FeS_2/MoS_2@RGO** can receive electrons from N_2 σ-orbital and offer electrons to the empty π*-orbital of N_2, causing enhanced adsorption of nitrogen species;[52] (ii) the strong interfacial interactions of both components (FeS_2 and MoS_2) can build many highspeed electron transport channels and lead an electronic coupling effect, hence promoting the activity by speeding up the electron transfer and optimizing the free energies of reaction intermediates[53]; (iii) the excellent electrical conductivity of graphene further facilitates the electrons transmission and improved the stability of electrodes.

Conclusions

In this work we have successfully constructed the heterostructure electrocatalyst of **FeS_2/MoS_2@RGO** derived from a polyoxometalate-containing MOF: PMo_{12}@MIL-100(Fe). The **FeS_2/MoS_2@RGO** composite displays a high Faradaic efficiency for electrocatalytic NRR due to the inherent electrochemical characteristics of the three components (FeS_2, MoS_2 and RGO) and to the efficient interface interaction and homogeneous distribution of the nanoparticles in the final composite. In an acidic 1.0 M K_2SO_4 electrolyte, **FeS_2/MoS_2@RGO** (15 % wt) reached the best performance with a FE of 38.6 % and a NH_3 yield ratio of 41.1 μg h^{-1} mg_{cat}^{-1} at -0.2 *vs*. RHE. Moreover, this catalyst showed a strong electrochemical durability for electrochemical NH_3 production, ranking it at the forefront in the field. This work may establish new possibilities to probe bioinspired multiple-component FeMoS containing compounds for efficient NRR electrocatalysis.

Conflicts of interest

There are no conflicts to declare.

Acknowledgements

This work was supported by Major Research Plan National Natural Science Foundation of China (Grant 92061102), the National Natural Science Foundation of China (Grant No. 22171059), the Outstanding Youth Project of Natural Science Foundation in Heilongjiang Province (YQ2020B005), Opening Foundation of Key Laboratory of Functional Inorganic Material Chemistry (Heilongjiang University, Ministry of Education), and the University Nursing Program for Young Scholars with Creative Talents in Heilongjiang Province (UNPYSCT-2018213).

References

[1] V. Smil, Detonator of the Population explosion, Nature 400 (1999) 415–415, https://doi.org/ 10.1038/22672.

[2] R. Schlogl, Catalytic synthesis of ammonia-a “never-ending story”?, Angew. Chem. Int. Ed. 42 (2003) 2004–2008, https://doi.org/ 10.1002/anie.200301553.

[3] J.-X. Feng, H. Pan, Electronic state optimization for electrochemical N_2 reduction reaction in aqueous solution, J. Mater. Chem. A 8 (2020) 13896–13915, https://doi.org/10.1039/D0TA04709K.

[4] Y.-W. Ren, C. Yu, X.-Y. Tan, H.-L. Huang, Q.-B. Wei, J.-S. Qiu, Strategies to suppress hydrogen evolution for highly selective electrocatalytic nitrogen reduction: challenges and perspectives, Energy Environ. Sci. 14 (2021) 1176–1193, https://doi.org/10.1039/D0EE03596C.

[5] C.J.M. Vanderham, M.T.M Koper, D.G.H Hetterscheid, Challenges in reduction of dinitrogen by proton and electron transfer, Chem. Soc. Rev. 43 (2014) 5183–5191, https://doi.org/10.1039/C4CS00085D.

[6] K.A. Brown, D.F. Harris, M.B. Wilker, A. Rasmussen, N. Khadka, H. Hamby, S. Keable, G. Dukovic, J.W. Peters, L.C. Seefeldt, P.W. King, Light-Driven dinitrogen reduction catalyzed by a CdS: nitrogenase MoFe protein biohybrid, Science 352 (2016) 448–450, https://doi.org/10.1126/science.aaf2091

[7] R.D. Milton, S. Abdellaoui, S.D. Minteer, N. Khadka, D.R. Dean, D. Leech, L.C. Seefedt, S.D. Minteer, Nitrogenase bioelectrocatalysis: heterogeneous ammonia and hydrogen production by MoFe protein, Energ. Environ. Sci. 9 (2016) 2550–2554, https://doi.org/10.1039/C6EE01432A.

[8] T. Oshikiri, K. Ueno, H. Misawa, Selective dinitrogen conversion to ammonia using water

and visible light through plasmon-induced charge separation, Angew. Chem. Int. Ed. 55 (2016) 3942–3946, https://doi.org/10.1002/anie.201511189.

[9] Y. Liu, H.-Y. Bai, Q.-X. Zhang, Y.-J. Bai, X.-L. Pang, F.-G. Wang, Y.-C. Yang, J.-R. Ding, W.-Q. Fan, W.-D. Shi, In-situ decoration of unsaturated Cu sites on Cu_2O photocathode for boosting nitrogen reduction reaction, Chem. Eng. J. 413 (2021) 127453, https://doi.org/10.1016/j.cej.2020.127453.

[10] B. Vedhanarayanan, C.-C. Chiu, J. Regner, Z. Sofer, K.C.S. Lakshmi, J.-Y. Lin, T.-W. Lin, Highly exfoliated $NiPS_3$ nanosheets as efficient electrocatalyst for high yield ammonia production, Chem. Eng. J. 430 (2022) 132649, https://doi.org/10.1016/j.cej.2021.132649.

[11] N.C. Kani, A.P. Prajapati, B.A. Collins, J.D. Goodpaster, M.R. Singh, Competing effects of pH, cation identity, H_2O saturation, and N_2 concentration on the activity and selectivity of electrochemical reduction of N_2 to NH_3 on electrodeposited Cu at ambient conditions, ACS Catal. 10 (2020) 14592−14603, https://doi.org/10.1021/acscatal.0c04864.

[12] M.-M. Shi, D. Bao, B.-R. Wulan, Y.-H. Li, Y.-F. Zhang, J.-M. Yan, Q. Jiang, Au sub-nanoclusters on TiO_2 toward highly efficient and selective electrocatalyst for N_2 conversion to NH_3 at ambient conditions, Adv. Mater. 29 (2017) 0935–9648, https://doi.org/10.1002/adma.201606550.

[13] R. Hao, W.-M. Sun, Q. Liu, X.-L. Liu, J.-L. Chen, X.-W. Lv, W. Li, Y.-P. Liu, Z.R. Shen, Efficient electrochemical nitrogen fixation over isolated Pt sites, Small 16 (2020) 1613–6810, https://doi.org/10.1002/smll.202000015.

[14] V. Kordali, G. Kyriacou, C. Lambbou, Electrochemical synthesis of ammonia at atmospheric pressure and low temperature in a solid polymer electrolyte cell, Chem. Commun. 17 (2000) 1673–1674, https://doi.org/10.1039/B004885M.

[15] H.-M. Liu, S.-H. Han, Y. Zhao, Y.-Y. Zhu, X.-L. Tian, J.-H. Zeng, J.-X. Jiang, B. Xia, Y. Chen, Surfactant-free atomically ultrathin rhodium nanosheet nano assemblies for efficient nitrogen electroreduction, J. Mater. Chem. A 6 (2018) 3211–3217, https://doi.org/10.1039/C7TA10866D.

[16] H.-Y. Wang, J.-T. Ren, C.-C. Weng, X.-W. Lv, Z.-Y. Yuan, Insight into the valence state of sisal-like MoO_2 nanosheet arrays for N_2 electrolysis, Chem. Eng. J. 46 (2021) 130761, https://doi.org/10.1016/j.cej.2021.130761.

[17] R. Zhang, Y. Zhang, X. Ren, G.-W. Gui, A.M. Asiri, B.-Z. Zheng, X.-P. Sun, High-efficiency electrosynthesis of ammonia with high selectivity under ambient conditions enabled by VN nanosheet array, ACS Sustain. Chem. Eng. 6 (2018) 9545–9549, https://doi.org/10.1021/acssuschemeng.8b01261.

[18] C. Lv, C.-S. Yan, G. Chen, Y. Ding, J.-X. Sun, Y.-S. Zhou, G.-H. Yu, An amorphous

noble-metal-free electrocatalyst that enables nitrogen fixation under ambient conditions, Angew. Chem. Int. Ed. 57 (2018) 6073–6076, https://doi.org/10.1002/anie.201801538.

[19] H. Cheng, L.-X. Ding, G.-F. Chen, L. Zhang, J. Xue, H. Wang, Molybdenum carbide nanodots enable efficient electrocatalytic nitrogen fixation under ambient conditions, Adv. Mater. 30 (2018) 0935–9648, https://doi.org/10.1002/adma.201803694.

[20] L. Zhang, X.-Q. Ji, X. Ren, Y.-J. Ma, X.-F. Shi, Z.-Q. Tian, A.M. Asiri, L. Chen, B. Tang, X.-P. Sun, Electrochemical ammonia synthesis via nitrogen reduction reaction on a MoS_2 catalyst: theoretical and experimental studies, Adv. Mater. 30 (2018) 0935–9648, https://doi.org/10.1002/adma.201800191.

[21] Z.-M. Zhao, S. Luo, P. Ma, Y.-T. Luo, W. Wu, Y. Long, J.-T. Ma, In situ synthesis of MoS_2 on C_3N_4 to form MoS_2/C_3N_4 with interfacial Mo−N coordination for electrocatalytic reduction of N_2 to NH_3, ACS Sustainable Chem. Eng. 8 (2020) 8814−8822, https://doi.org/10.1021/acssuschemeng.0c02763.

[22] K. Chu, Y.-P. Liu, Y.-B. Li, Y.-L. Guo, Y. Tian, Two-dimensional (2D)/2D Interface engineering of a MoS_2/C_3N_4 heterostructure for promoted electrocatalytic nitrogen fixation, ACS Appl. Mater. Interfaces 12 (2020) 7081−7090, https://doi.org/10.1021/acsami.9b18263.

[23] B.H.R. Suryanto, D. Wang, L.M. Azofra, M. Harb, L.G. Cavallo, R. Jalili, D.R.G. Mitchell, M. Chatti, D.R. MacFarlane, MoS_2 polymorphic engineering enhances selectivity in the electrochemical reduction of nitrogen to ammonia, ACS Energy Lett. 4 (2019) 430–435, https://doi.org/10.1021/acsenergylett.8b02257.

[24] Y.-Y. Liu, W.-K. Wang, S.-B. Zhang, W.-L. Li, G.-Z. Wang, Y.-X. Zhang, M.-M. Han, H.-M. Zhang, MoS_2 nanodots anchored on reduced graphene oxide for efficient N_2 fixation to NH_3, ACS Sustainable Chem. Eng. 8 (2020) 2320–2326, https://doi.org/10.1021/acssuschemeng.9b07679.

[25] B.K. Burgess, D.J. Lowe, Mechanism of molybdenum nitrogenase, Chem. Rev. 96 (1996) 2983–3012, https://doi.org/10.1021/cr950055x.

[26] M.-L. Cheng, X.-F. Zhang, Y. Zhu, M. Wang, Selective photocatalytic reduction of CO_2 to CO mediated by a [FeFe]-hydrogenase model with a 1,2-phenylene S-to-S bridge, Chinese J. Catal. 42 (2021) 310–319, https://doi.org/10.1016/S1872-2067(20)63644-0.

[27] R. Zhang, X. Ren, X.-F. Shi, F.-Y. Xie, B.-Z. Zheng, X.-D. Guo, X.-P. Sun, Enabling effective electrocatalytic N_2 conversion to NH_3 by the TiO_2 nanosheets array under ambient conditions, ACS Appl. Mater. Interfaces 10 (2018) 28251–28255, https://doi.org/10.1021/acsami.8b06647.

[28] A. Bavykina, N. Kolobov, II.S. Khan, J.A. Bau, A. Ramirez, J. Gascon, Metal−organic frameworks in heterogeneous catalysis: recent progress, new trends, and future perspectives,

Chem. Rev. 120 (2020) 8468−8535, https://doi.org/10.1021/acs.chemrev.9b00685.

[29] Y.-J. Tang, M.-R. Gao, C.-H. Liu, S.-L. Li, H.-L. Jiang, Y.-Q. Lan, M. Han, S.-H. Yu, Porous molybdenum-based hybrid catalysts for highly efficient hydrogen evolution, Angew. Chem. Int. Ed. 127 (2015) 13120–13124, https://doi.org/10.1002/ange.201505691.

[30] J.-S. Li, Y.-J. Tang, C.-H. Liu, S.-L. Li, R.-H. Li, L.-Z. Dong, Z.-H. Dai, J.-C. Bao, Y.-Q. Lan, Polyoxometalate-based metal–organic framework derived hybrid electrocatalysts for highly efficient hydrogen evolution reaction, J. Mater. Chem. A 4 (2016) 1202–1207, https://doi.org/10.1039/C5TA09743F.

[31] J.-H. Duan, D.-Z. Shao, W.-W. Wang, D.-L. Zhang, C.-J. Li, Strongly coupled molybdenum phosphide@phosphorus-doped porous carbon derived from MOF used in N_2 electroreduction under ambient conditions, Micropor. Mesopor. Mat. 313 (2021) 1387-1811, https://doi.org/10.1016/j.micromeso.2020.110852.

[32] N. Li, J. Liu, B.-X. Dong, Y.-Q. Lan, Polyoxometalate-based compounds for photo-and electrocatalytic applications, Angew. Chem. Int. Ed. 59 (2020) 20779-20793, https://doi.org/10.1002/anie.202008054

[33] J. Yu, Y.-N. Guo, S.-S. Miao, M. Ni, W. Zhou, Z.-P. Shao, Spherical ruthenium disulfide-sulfur-doped graphene composite as an efficient hydrogen evolution electrocatalyst, ACS Appl. Mater. Interfaces 10 (2018) 34098−34107, https://doi.org/10.1002/anie.202008054.

[34] J. Zhang, Y.-J. Ji, P.-T. Wang, Q. Shao, Y.-Y. Li, X.-Q. Huang, Adsorbing and activating N_2 on heterogeneous Au–Fe_3O_4 nanoparticles for N_2 fixation, Adv. Funct. Mater. 30 (2019) 1616-301X, https://doi.org/10.1002/adfm.201906579.

[35] J.-W. Su, R.-X. Ge, Y. Dong, F. Hao, L. Chen, Recent progress in single-atom electrocatalysts: concept, synthesis, and applications in clean energy conversion, J. Mater. Chem. A 6 (2018) 14025–14042, https://doi.org/10.1039/C8TA04064H.

[36] L. Hu, Z. Xing, X.-F. Feng, Understanding the electrocatalytic interface for ambient ammonia synthesis, ACS Energy Lett. 5 (2020) 430−436, https://doi.org/10.1021/acsenergylett.9b02679.

[37] G.-N. Wang, T.-T. Chen, C.J. Gómez-García, F. Zhang, M.-Y. Zhang, H.-Y. Ma, H.-J. Pang, X.-M. Wang, L.-C. Tan, A high-capacity negative electrode for asymmetric supercapacitors based on a PMo_{12} coordination polymer with novel water-assisted proton channels, Small. 16 (2020) 1613-6810, https://doi.org/10.1002/smll.202001626.

[38] J.-H. Duan, D.-Z. Shao, W.-W. Wang, D.-L. Zhang, C.-J. Li, Strongly coupled molybdenum phosphide@phosphorus-doped porous carbon derived from MOF used in N_2 electroreduction under ambient conditions, Micropor. Mesopor. Mat. 313 (2021) 1387–1811,

https://doi.org/10.1016/j.micromeso.2020.110852.

[39] X.-M. Wang, Z.-M. Feng, B.-X. Xiao, J.-X. Zhao, H.-Y. Ma, Y. Tian, H.-J. Pang, L.-C. Tan, Polyoxometalate-based metal-organic framework-derived bimetallic hybrid materials for upgraded electrochemical reduction of nitrogen, Green Chem. 22 (2020) 6157–6169, https://doi.org/10.1039/D0GC01149E.

[40] Q.-B. Shen, C.J. Gomez-Garcia, W.-L. Sun, X.-Y. Lai, H.-J. Pang, H.-Y. Ma, Improving the photocatalytic H_2 evolution activity of keggin polyoxometalates anchoring copper-azole complexes, Green Chem.23 (2021) 3104-3114, https://doi.org/10.1039/D1GC00692D.

[41] S.-B. Li, X.-G. Tan, M. Yue, L. Zhang, D.-F. Chai, W.-D. Wang, H. Pan, L.-L. Fan, C.-Y. Zhao, A polyoxometalate-encapsulated nanocage cluster organic framework built from $\{Cu_4P_2\}$ units and its efficient bifunctional electrochemical performance, Chem. Commun. 56 (2020) 15177–15180, https://doi.org/10.1039/D0CC06665F.

[42] J.-S. Li, S. Zhang, J.-Q. Sha, H. Wang, M.-Z. Liu, L.-X. Kong, G.-D. Liu, Confined molybdenum phosphide in p-doped porous carbon as efficient electrocatalysts for hydrogen evolution, ACS Appl. Mater. Interfaces 10 (2018) 17140–17146, https://doi.org/10.1021/acsami.8b01541.

[43] B.-R. Lu, S.-B. Li, J. Pan, L. Zhang, J.-J. Xin, Y. Chen, X.-G. Tan, pH-controlled assembly of five new organophosphorus strandberg-type cluster-based coordination polymers for enhanced electrochemical capacitor performance, Inorg. Chem. 59 (2020) 1702–1714, https://doi.org/10.1021/acs.inorgchem.9b02858.

[44] Y. Wang, X.-Q. Cui, J.-X. Zhao, G.-R. Jia, L. Gu, Q.-H. Zhang, L.-K. Meng, Z. Shi, L.-R. Zheng, C.-Y. Wang, Z.-W. Zhang, W.-T. Zheng, Rational design of Fe-N/C hybrid for enhanced nitrogen reduction electrocatalysis under ambient conditions in aqueous solution, ACS Catal. 9 (2019) 336–344, https://doi.org/10.1021/acscatal.8b03802.

[45] W. Ye, M. Arif, X.-Y. Fang, M.A. Mushtaq, X.-B. Chen, D.-P. Yan, Efficient photoelectrochemical route for the ambient reduction of N_2 to NH_3 based on nanojunctions assembled from MoS_2 nanosheets and TiO_2, ACS Appl. Mater. Interfaces 11 (2019) 28809−28817, https://doi.org/10.1021/acsami.9b06596.

[46] D. Zhu, Q.-F. Zhen, J.-J. Xin, H.-Y. Ma, L.-C. Tan, H.-J. Pang, X.-M. Wang, A free-standing and flexible phosphorus/nitrogen dual-doped three-dimensional reticular porous carbon frameworks encapsulated cobalt phosphide with superior performance for nitrite detection in drinking water and sausage samples, Sensor. Actuat. B-Chem. 321 (2020) 128541, https://doi.org/10.1016/j.snb.2020.128541.

[47] Y.-J. Tang, Y. Wang, X.-L. Wang, S.-L. Li, W. Huang, L.-Z. Dong, C.-H. Liu, Y.-F. Li, Y.-Q. Lan, Molybdenum disulfide/nitrogen-doped reduced graphene oxide nanocomposite

with enlarged interlayer spacing for electrocatalytic hydrogen evolution, Adv. Energy. Mater. 6 (2016) 1614-6832, https://doi.org/10.1002/aenm.201600116.

[48] H.-J. Yu, Z.-Q. Wang, S.-L. Yin, C.-J. Li, Y. Xu, X.-N. Li, L. Wang, H.-J. Wang, Mesoporous Au_3Pd film on Ni foam: a self-supported electrocatalyst for efficient synthesis of ammonia, ACS Appl. Mater. Interfaces 12 (2020) 436–442, https://doi.org/10.1021/acsami.9b14187.

[49] H.-J. Wang, Y.-H. Li, C.-J. Li, K. Deng, Z.-Q. Wang, Y. Xu, X.-N. Li, H.-R. Xue, L. Wang, One-pot synthesis of Bi-metallic PdRu tripods as an efficient catalyst for electrocatalytic nitrogen reduction to ammonia, J. Mater. Chem. A 7 (2019) 801–805, https://doi.org/10.1039/C8TA09482A.

[50] H. Tao, C. Choi, L.-X. Ding, Z. Jiang, Z. Han, M. Jia, Q. Fan, Y. Gao, H. Wang, A.W. Robertson, S. Hong, Y. Jung, S. Liu, Z. Sun, Nitrogen fixation by Ru single-atom electrocatalytic reduction, Chem. 5 (2019) 204–214, https://doi.org/10.1016/j.chempr.2018.10.007.

[51] S.-L. Chen, H. Jang, J. Wang, Q. Qin, X. Liu, J. Cho, Bimetallic metal-organic framework-derived MoFe-PC microspheres for electrocatalytic ammonia synthesis under ambient conditions, J. Mater. Chem. A 8 (2020) 2099–2104, https://doi.org/10.1039/C9TA10524G.

[52] Y.-C. Hao, Y. Guo, L.-W. Chen, M. Shu, X.-Y. Wang, T.-A. Bu, W.-Y. Gao, N. Zhang, X. Su, X. Feng, J.-W. Zhou, B. Wang, C.-W. Hu, A.-X. Yin, R. Si, Y.-W. Zhang, C.-H. Yan, Promoting nitrogen electroreduction to ammonia with bismuth nanocrystals and potassium cations in water, Nat. Catal. 2 (2019) 467–467, https://doi.org/10.1038/s41929-019-0241-7.

[53] M.A. Lukowski, A.S. Daniel, F. Meng, A. Forticaux, L.-S. Li, S. Jin, Enhanced hydrogen evolution catalysis from chemically exfoliated metallic MoS_2 nanosheets, J. Am. Chem. Soc. 135 (2013) 10274–10277, https://doi.org/10.1021/ja404523s.

Declaration of interests

☒ The authors declare that they have no known competing financial interests or personal relationships that could have appeared to influence the work reported in this paper.

☐The authors declare the following financial interests/personal relationships which may be considered as potential competing interests:
